PHYSICS

Local Berry curvature signatures in dichroic angle-resolved photoelectron spectroscopy from two-dimensional materials

Michael Schüler[1,2]*, Umberto De Giovannini[3], Hannes Hübener[3], Angel Rubio[3,4], Michael A. Sentef[3], Philipp Werner[2]

Topologically nontrivial two-dimensional materials hold great promise for next-generation optoelectronic applications. However, measuring the Hall or spin-Hall response is often a challenge and practically limited to the ground state. An experimental technique for tracing the topological character in a differential fashion would provide useful insights. In this work, we show that circular dichroism angle-resolved photoelectron spectroscopy provides a powerful tool that can resolve the topological and quantum-geometrical character in momentum space. In particular, we investigate how to map out the signatures of the momentum-resolved Berry curvature in two-dimensional materials by exploiting its intimate connection to the orbital polarization. A spin-resolved detection of the photoelectrons allows one to extend the approach to spin-Chern insulators. The present proposal can be extended to address topological properties in materials out of equilibrium in a time-resolved fashion.

INTRODUCTION

The discovery of the remarkable physical consequences of the Berry curvature of wave functions in materials has spurred progress across many research fields in physics. In periodic solids, the most notable examples are topological insulators (TIs) and superconductors (*1*, *2*), in which a global topological invariant emerges from momentum-space integrals of the Berry curvature. This global topology gives rise, for example, to a quantized Hall conductance carried by surface or edge states (*1*). In particular, two-dimensional (2D) systems are currently in the spotlight for their flexibility in creating van der Waals heterostructures and thus potentially next-generation transistor devices (*3*). However, independently of the global topology, it is becoming increasingly evident that the local (in momentum space) quantum geometry can have dramatic physical consequences as well. Haldane (*4*) pointed out the consequence of Berry curvature on the Fermi surface for Fermi-liquid transport properties, reinterpreting the Karplus-Luttinger anomalous velocity (*5*) in modern Berry phase language. Similarly, a geometrical description of the fractional quantum Hall effect was proposed (*6*). Examples of physical consequences of quantum geometry, expressed as the Fubini-Study metric, include unusual current-noise characteristics (*7*) or the geometric origin of superfluidity in flat-band systems (*8*). Other prominent examples for the impact of local Berry curvature are strongly anisotropic high-harmonic generation signals from hexagonal boron nitride (hBN) or transition-metal dichalogenides (TMDC) (*9*, *10*) and the valley Hall effect (*11*). Also, the recently discovered nonlinear Hall effect (*12*–*14*) in topologically trivial systems is an important manifestation of local Berry curvature effects.

In contrast to cold atoms in optical lattices, where measurements of the local Berry curvature were recently demonstrated (*15*), the observation of the local Berry curvature in materials still poses a challenge. Although remarkable progress (*16*–*18*) in predicting and realizing large-gap 2D TIs has been made, alternative efficient ways of exploring topological properties are necessary to further advance this active branch of materials research. Recent theoretical proposals (*19*, *20*) and experimental realizations (*21*) in ultracold atomic gases have demonstrated a quantization of circular dichroism in the photoabsorption, which enables a clear distinction between topologically trivial and nontrivial phases. Similarly, dichroic selection rules determine the optical absorption of 2D materials, especially in the presence of excitons (*22*). The underlying mechanism is—similar to magnetic systems (*23*)—the intrinsic orbital angular momentum and the resulting orbital polarization. In this work, we demonstrate that the extension of this approach to angle-resolved photoemission (ARPES) with circularly polarized light provides direct information on the Berry curvature in 2D systems. Unlike photoabsorption, the circular dichroism in the angular distribution is sensitive to the momentum-resolved orbital polarization and thus gives access to valley-resolved topological properties. This enables tracing the local Berry curvature, which is hardly accessible by other experimental techniques.

We demonstrate the connection between circular dichroism, orbital polarization, and the Berry curvature by considering simple tight-binding (TB) models and confirm our findings by state-of-the-art ab initio calculations based on real-time time-dependent density functional theory (TDDFT) (*24*). The latter formalism provides a realistic description of the full ionization process including final-state effects, transport through the material, electron-electron interaction, and nonequilibrium effects (*25*–*28*). While we will focus the discussion on paradigmatic systems similar to graphene, our results are generic and can be applied to other 2D materials.

RESULTS

Berry curvature and orbital angular momentum

Orbital polarization and the resulting orbital magnetization are fundamental properties of the Bloch wave functions of individual bands

[1]Stanford Institute for Materials and Energy Sciences (SIMES), SLAC National Accelerator Laboratory, Menlo Park, CA 94025, USA. [2]Department of Physics, University of Fribourg, 1700 Fribourg, Switzerland. [3]Max Planck Institute for the Structure and Dynamics of Matter, Luruper Chaussee 149, 22761 Hamburg, Germany. [4]Center for Computational Quantum Physics (CCQ), The Flatiron Institute, 162 Fifth Avenue, New York, NY 10010, USA.
*Corresponding author. Email: schuelem@stanford.edu

and have an intimate connection to the Berry curvature. To illustrate this relation and its manifestation in ARPES, let us consider a generic 2D material, possibly with spin-orbit coupling (SOC). We focus on the case where the z-projection of the spin S_z is still an exact quantum number in the relevant parts of the Brillouin zone (BZ), even in the presence of SOC. This assumption is typically valid if the atomic SOC is the dominant contribution and the relevant orbitals are directed in-plane or out of plane. This includes the typical case of π and σ electron systems (*17*), as studied below, as well as 2D TMDCs (*29*). Hence, we consider the general Bloch Hamiltonian in the spinor basis

$$\hat{H}(\mathbf{k}) = \begin{pmatrix} \hat{h}_{\uparrow}(\mathbf{k}) & 0 \\ 0 & \hat{h}_{\downarrow}(\mathbf{k}) \end{pmatrix} \tag{1}$$

The conservation of S_z can be broken by structural deviations from 2D geometry (affecting the next–nearest-neighbor SOC) and orbital hybridization (like π − σ hybridization). However, the Hamiltonian (Eq. 1) provides an excellent approximation for the systems investigated here. The validity of this description is supported by the analysis in section S1.

In the absence of magnetism, time-reversal symmetry (TRS) holds, constraining $\hat{h}_{\downarrow}(\mathbf{k}) = [\hat{h}_{\uparrow}(-\mathbf{k})]^*$ and giving rise to a degeneracy of the spin-resolved bands: $\hat{h}_{\sigma}(\mathbf{k})|u_{\mathbf{k}\alpha\sigma}\rangle = \varepsilon_{\mathbf{k}\alpha}|u_{\mathbf{k}\alpha\sigma}\rangle$. The individual bands have intrinsic properties, which are determined by the band structure topology. An important example of such properties is the orbital polarization. The full description of angular momentum and the related orbital magnetization in terms of the Berry phase theory (*30*) (so-called modern theory of polarization) has been formulated relatively recently. For a band α with spin σ, the orbital moment is defined as

$$\ell^z_{\alpha\sigma}(\mathbf{k}) = \frac{m}{\hbar}\mathrm{Im}\langle \partial_{k_x} u_{\mathbf{k}\alpha\sigma}|\hat{h}_{\sigma}(\mathbf{k}) - \varepsilon_{\mathbf{k}\alpha}|\partial_{k_y} u_{\mathbf{k}\alpha\sigma}\rangle \tag{2}$$

This shows that the orbital magnetization $m_z(\mathbf{k}) = (e/m)\,\ell^z_{\alpha\sigma}(\mathbf{k})$ is an intrinsic property of the underlying band, related to self-rotation, which can emerge even if no magnetic atoms are present.

In general, the orbital moment (Eq. 2) is composed of a term proportional to the Berry curvature $\Omega_{\nu\sigma}(\mathbf{k})$ and a correction term (*31*). Moreover, in the typical case where the Berry curvature is predominantly due to the hybridization of two participating orbitals, forming the valence (v) and conduction (c) band, the orbital polarization of the valence band becomes

$$\ell^z_{\nu\sigma}(\mathbf{k}) = -\frac{m}{\hbar}(\varepsilon_{\mathbf{k}c} - \varepsilon_{\mathbf{k}v})\,\Omega_{\nu\sigma}(\mathbf{k}) \tag{3}$$

TRS implies $\Omega_{v\uparrow}(\mathbf{k}) = -\Omega_{v\downarrow}(-\mathbf{k})$, while inversion symmetry results in $\Omega_{v\uparrow}(\mathbf{k}) = \Omega_{v\uparrow}(-\mathbf{k})$. Hence, in systems having both symmetries, $\Omega_{v\uparrow}(\mathbf{k}) = -\Omega_{v\downarrow}(\mathbf{k})$ holds; in the absence of SOC, the Berry curvature and thus the orbital polarization vanish exactly. Therefore, measuring the momentum-resolved orbital polarization allows one to map out the local Berry curvature. While Eq. 3 is exact for two-band systems, it is still a good approximation for multiband systems in the vicinity of high-symmetry points. Selecting the dominant bands based on the size of hybridization gaps and dipole selection rules still allows one to approximately determine the Berry curvature from a relation like Eq. 3. This is exemplified in section S2.

For graphene-like insulating systems, the Berry curvature and the orbital polarization for the three possible scenarios are shown in Fig. 1. Graphene (neglecting the SOC) has inversion symmetry, and respective sublattice sites on the honeycomb lattice are equivalent; hence $\ell^z(\mathbf{k})$ is zero in both spin channels, giving rise to a Dirac semimetal. Breaking inversion symmetry—for instance, by considering systems with inequivalent atoms on the respective sublattice sites as in hBN—opens a gap and generates a nonzero Berry curvature. The resulting trivial insulator exhibits orbital polarization at the Dirac points K and K′ with opposite sign due to TRS. The system is characterized by a nonzero valley Chern number $C_{\mathrm{val}}(K) = -C_{\mathrm{val}}(K') = \int_{\mathrm{val}(K)} d\mathbf{k}\,\Omega_v(\mathbf{k})/2\pi$, indicating a pronounced valley magnetization.

SOC in graphene-like systems renders them (type II) Z_2 spin-Chern insulators (*1*), according to the Kane-Mele mechanism (*32*). The bands exhibit an inverted orbital character at K and K′, respectively, while the TRS is broken for each spin channel individually (although the system has global TRS). Considering the total angular momentum, the spin-Chern number $C_s = \pm 1$ indicates a total chiral $L_z = \int d\mathbf{k}\,\ell^z(\mathbf{k}) \neq 0$, with the same magnitude and opposite sign for spin-up and spin-down electrons, respectively.

While optical techniques sensitive to a total chirality—such as magnetic circular dichroism (MCD)—cannot separate out the individual spin channels, advances in spin-resolved ARPES (sARPES) (*33*) enable a selective measurement of spin-up or spin-down photoelectrons. A dichroic sARPES measurement would allow one to map out momentum- and spin-resolved orbital properties, which is hard to achieve by other methods. Recent experiments on chiral surface states in TIs (*34*, *35*) and TMDCs (*36*–*38*) demonstrate the feasibility of detecting circular dichroism in photoemission. In particular, the possibility to map out the valley-specific orbital polarization and its connection to the spin polarization has already been demonstrated for bulk MoS_2 (*37*) and bulk *2H*-WSe_2 (*38*).

Circular dichroism in sARPES and ARPES

To discuss how the orbital polarization is reflected in ARPES, we consider the photoemission intensity as described by Fermi's golden rule in the dipole approximation (*39*)

$$I(\mathbf{p}, \varepsilon_f) \propto |\langle \chi_{\mathbf{p},p_\perp}|\hat{\epsilon}\cdot\hat{D}|\psi_{\mathbf{k}\alpha}\rangle|^2 \delta(\varepsilon_{\mathbf{p}\alpha} + \hbar\omega - \varepsilon_f) \tag{4}$$

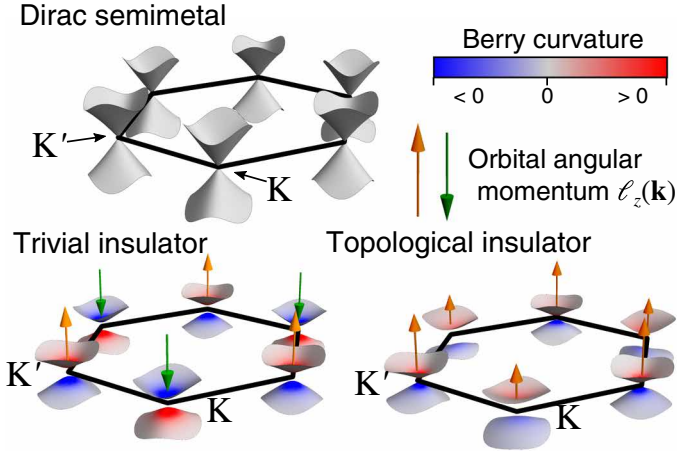

Fig. 1. Illustration of the Berry curvature and orbital angular momentum. The surfaces represent the valence and conduction band, while the coloring indicates the Berry curvature. The arrows illustrate the orbital angular momentum of the valence band.

where $|\psi_{\mathbf{k}\alpha}\rangle$ denotes the Bloch state corresponding to the cell-periodic wave function $|u_{\mathbf{k}\alpha}\rangle$. The photon energy is given by $\hbar\omega$, and $\varepsilon_f = (\mathbf{p}^2 + p_\perp^2)/2$ is the energy of the photoelectron final state $|\chi_{\mathbf{p},p_\perp}\rangle$. The matrix element of the dipole operator $\hat{D}$ and the polarization direction $\hat{\epsilon}$ determine the selection rules. The in-plane momentum $\mathbf{p}$ is identical to the quasi-momentum $\mathbf{k}$ up to a reciprocal lattice vector. We can extend Eq. 4 to the spin-resolved intensity $I_\sigma(\mathbf{p}, \varepsilon_f)$ by assuming a spin-resolved detection of the final states $|\chi_{\mathbf{p},p_\perp,\sigma}\rangle$, fixing the photoelectron spin σ.

To detect orbital textures, we exploit the circular dichroism in ARPES (CD-ARPES). As shown in Fig. 2A, we consider the experimental situation, where the probe field is either left-hand circularly polarized (LCP) or right-hand circularly polarized (RCP), with the polarization vector $\hat{\epsilon}^{(\pm)}$ in-plane, i.e., normal incident fields. Although tilting the incident direction by small angles, as is often the case in experiments, introduces an additional small contribution to the circular dichroism, we expect that the qualitative behavior is not affected. The corresponding CD-ARPES intensities $I^{(\pm)}(\mathbf{k}, \varepsilon_f)$ then define the total (unpolarized) $I_{\mathrm{tot}}(\mathbf{k}, \varepsilon_f) = I^{(-)}(\mathbf{k}, \varepsilon_f) + I^{(+)}(\mathbf{k}, \varepsilon_f)$ and circular dichroism $I_{\mathrm{CD}}(\mathbf{k}, \varepsilon_f) = I^{(-)}(\mathbf{k}, \varepsilon_f) - I^{(+)}(\mathbf{k}, \varepsilon_f)$ signal.

Connection to orbital polarization

The close connection between the dichroic signal $I_{\mathrm{CD}}(\mathbf{k}, \varepsilon_f)$ and the Berry curvature is already apparent from symmetry considerations. TRS dictates $I_{\mathrm{CD}}(\mathbf{k}, \varepsilon_f) = -I_{\mathrm{CD}}(-\mathbf{k}, \varepsilon_f)$, such that the circular dichroism integrated over the whole BZ vanishes. In addition, a system having inversion symmetry results in an exactly vanishing valley-integrated circular dichroism, analogous to the Berry curvature. This argument demonstrates that the breaking of TRS, a characteristic property of Chern insulators, is reflected in a nonzero total circular dichroism.

The manifestation of local orbital chirality in the circular dichroism can be understood intuitively in terms of the wave packet picture, which also plays a fundamental role in the theory of orbital magnetization (*30*). Instead of a Bloch initial state $|\psi_{\mathbf{k}\alpha}\rangle$, we can consider a wave packet $|W_{\mathbf{k}\alpha}\rangle$ composed of momenta close to $\mathbf{k}$. Hence, $W_{\mathbf{k}\alpha}(\mathbf{r})$ has a finite spread in real space and properties similar to a molecular orbital. In particular, its angular momentum is given by $\langle \hat{L}_z \rangle_{\mathbf{k}\alpha} = \langle W_{\mathbf{k}\alpha} | \hat{L}_z | W_{\mathbf{k}\alpha} \rangle$; in the limit of an infinitely sharp distribution, such that $|W_{\mathbf{k}\alpha}\rangle$ becomes identical to $|\psi_{\mathbf{k}\alpha}\rangle$, one finds $\langle \hat{L}_z \rangle_{\mathbf{k}\alpha} = \ell_\alpha^z(\mathbf{k})$. Nonzero $\langle \hat{L}_z \rangle_{\mathbf{k}\alpha}$ indicates self-rotation of the wave packet, which will be reflected in the dipole selection rules in the ARPES matrix elements in Eq. 4.

This picture can be used to obtain a qualitative description of the dichroism, as detailed in section S3. Introducing the analog of a cell-periodic function by $F_{\mathbf{k}\alpha}(\mathbf{r}) = e^{-i\mathbf{k}\cdot\mathbf{r}} W_{\mathbf{k}\alpha}(\mathbf{r})$, its magnetic properties can be analyzed by projecting it onto eigenfunctions of $\hat{L}_z$: $F_{\mathbf{k}\alpha}(\mathbf{r}) = 1/\sqrt{2\pi} \sum_m e^{im\theta} \mathcal{F}_{\mathbf{k}\alpha,m}(s,z)$, where (s, θ) are the in-plane polar coordinates. Replacing the final states by plane waves (PWs), one can approximate the matrix elements in Eq. 4 by

$$M_\alpha^{(\pm)}(\mathbf{k}, p_\perp) \approx \int_0^\infty ds \int_{-\infty}^\infty dz\, e^{-ip_\perp z} s^2 \mathcal{F}_{\mathbf{k}\alpha,\mp 1}(s,z) \qquad (5)$$

Therefore, the orbital polarization of the initial state is directly reflected in the circular dichroism. Except for some marginal cases, a nonzero value of $\ell_\alpha^z(\mathbf{k})$ gives rise to different weights with respect to the $\mathcal{F}_{\mathbf{k}\alpha,\pm 1}$ component. Moreover, $\ell_\alpha^z(\mathbf{k}) > 0$ ($\ell_\alpha^z(\mathbf{k}) < 0$) typically corresponds to a dominant contribution from $m = +1$ ($m = -1$). In contrast, $\ell_\alpha^z(\mathbf{k}) = 0$ is almost always equivalent to equal weights of $m = \pm 1$, which results in a vanishing circular dichroism. Therefore, the nodal lines of $\ell_\alpha^z(\mathbf{k})$ can be mapped out. For other regions in the BZ, the nonvanishing circular dichroism indicates $\ell_\alpha^z(\mathbf{k}) \neq 0$. Hence, the profile of $\ell_\alpha^z(\mathbf{k})$—and thus the Berry curvature—across the whole BZ can be obtained, up to a $\mathbf{k}$-dependent prefactor. In section S3, we discuss the illustrative example of hBN and analyze the orbital polarization in detail.

Calculation of photoemission spectra

To compute (CD-) ARPES from first principles, one does not need to resort to the approximated one-step model of photoemission like the one of Eq. 4. Instead of using Eq. 4, we use TDDFT (*40*) with the

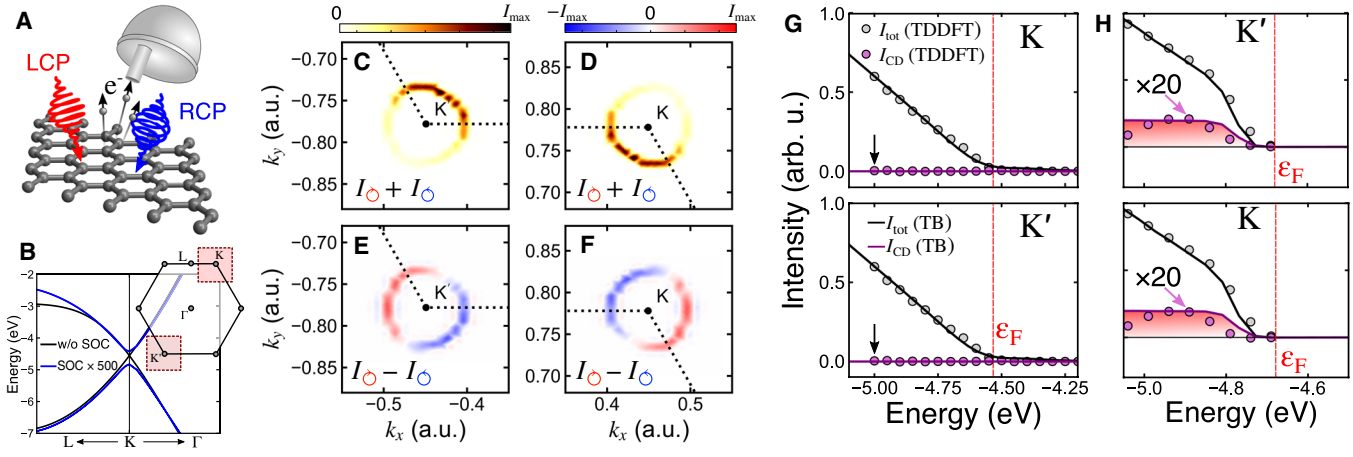

Fig. 2. Setup and circular dichroism in graphene. (**A**) Sketch of the calculation setup: photoemission by left-hand circularly polarized light (LCP) or right-hand circularly polarized light (RCP), with polarization vector in the plane. (**B**) Band structure of graphene close to the Dirac point with zero (black line) and enhanced (blue line) SOC, respectively, obtained from density functional theory (DFT). The first Brillouin zone (BZ) of the system with honeycomb lattice is shown in the inset. The shaded boxes indicate the magnified regions shown in (C) to (F). (**C** and **D**) Total ARPES intensity $I_{\mathrm{tot}}(\mathbf{k}, \varepsilon_f)$ (normalized to its maximum value $I_{\max}$) at $\varepsilon_f = 47$ eV, close to the K and K′ point, respectively. (**E** and **F**) Corresponding dichroic signal $I_{\mathrm{CD}}(\mathbf{k}, \varepsilon_f)$. The quasi-momentum is measured in atomic units (a.u.) (inverse Bohr). (**G**) Integrated signal [over the shaded regions in (B)] I_{tot} and I_{CD} as a function of the binding energy (circles, TDDFT results; lines, TB + PW model). The black arrow indicates the energy for which the angle-resolved intensities in (C) to (F) are shown. arb. u. (arbitrary units). (**H**) Integrated signal from spin-up electrons [analogous to (G)] for graphene with enhanced SOC.

t-SURFFP method (*24*), which avoids any reference to explicit final states by directly computing the momentum and energy distribution of the photocurrent created by a specific pulse field and thus allows computing the intensity directly from the real-time evolution.

While the first-principles approach provides results in excellent agreement with experiments (see below), a more intuitive understanding can be gained by considering a simple model for the direct evaluation of Eq. 4. The Bloch states are represented by a TB model of atomic orbitals, while replacing the final states $|\chi_{\mathbf{p},p_\perp}\rangle$ in this equation by PWs $|\mathbf{p},p_\perp\rangle$ eliminates scattering of the photoelectron from the lattice, which allows us to focus on the intrinsic contribution of the Bloch states to the ARPES intensity. The matrix elements in Eq. 4 are computed in the length gauge; i.e., the dipole operator entering the light-matter matrix elements is represented by the position operator **r** measured from each unit cell. This encodes the selection rules with respect to the LCP or RCP polarization. In what follows, we refer to the resulting model as the TB + PW model. Furthermore, an analytical treatment is possible in certain cases, providing a clear physical picture.

The combination of the two methods allows a comprehensive analysis. The details on both methods can be found in Materials and Methods and in section S4.

ARPES for typical materials

Here, we investigate the three classes of 2D materials represented in Fig. 1, namely, the Dirac semimetal, trivial insulator, and TI, and identify the distinct features in CD-ARPES. The Dirac semimetal we consider is graphene, while hBN exemplifies a trivial insulator. As examples of TIs, we study bismuthane and graphene with artificially enhanced SOC.

Graphene

We start by discussing ARPES from graphene, which is the prototype of a 2D material. We focus on the regions in the first BZ close to the two inequivalent Dirac points (Fig. 2B). The photon energy is fixed at $\hbar\omega = 52$ eV. Neglecting the very weak SOC, spin resolution is not required at this point.

Figure 2 (C and D) shows a typical ARPES cut at fixed ε_f, obtained by the t-SURFFP approach. Consistent with experiments (*41*), the prominent dark corridor (region of minimal intensity) is observed in the Γ-K or Γ-K′ direction at this photon energy. The dark corridor is a consequence of destructive interference of the emission from the two sublattice sites (*41*).

The calculated dichroic signal $I_{\mathrm{CD}}(\mathbf{k},\varepsilon_f)$, shown in Fig. 2 (E and F), is in very good agreement with the experimental data reported in (*42*). In particular, when following a path perpendicular to the Γ-K direction, the chiral character is consistent with the experimental data from (*43*). As is apparent from Fig. 2 (E and F), the valley-integrated circular dichroism vanishes. This is confirmed by both theoretical methods, shown in Fig. 2G, where we compare the integrated TDDFT results to those of the TB + PW model for an integration range corresponding to the two shaded regions in Fig. 2B, finding excellent agreement. Hence, the dichroic properties provide a direct proof of the vanishing Berry curvature.

Hexagonal boron nitride

We now turn to the paradigmatic case of a trivial insulator with broken inversion symmetry (as shown in Fig. 1) by studying single-layer hBN. Similar to graphene, hBN is a π-conjugated system dominated by p_z orbitals on the sublattice sites with a large ionic-like band gap. The Berry curvature becomes finite and very pronounced around the K and K′ points. Comparing $\Omega_\nu(\mathbf{k})$ of the top valence band within the TB model and the first-principles calculation (Fig. 3A), the excellent agreement indicates that the orbital mixing of the top valence and bottom conduction band—of predominant p_z orbital character—gives the main contribution to $\Omega_\nu(\mathbf{k})$. Hence, Berry curvature and angular momentum $\ell_z(\mathbf{k})$ are proportional to each other, cf. Eq. 3. The valley-integrated angular momentum is $L_z \approx \pm 0.1$ with opposite sign at K and K′, respectively (Fig. 3A). We have also explicitly evaluated wave packets and the associated OAM in section S3. The prediction of the dichroism from Eq. 5 is qualitatively in line with the calculated circular dichroism in Fig. 3 (D and E).

The valley-resolved measurement provided by CD-ARPES, as opposed to MCD (*23*), allows one to trace the valley polarization. Because of the direct link to the local Berry curvature (Eq. 4), this provides a way of measuring the valley Chern number.

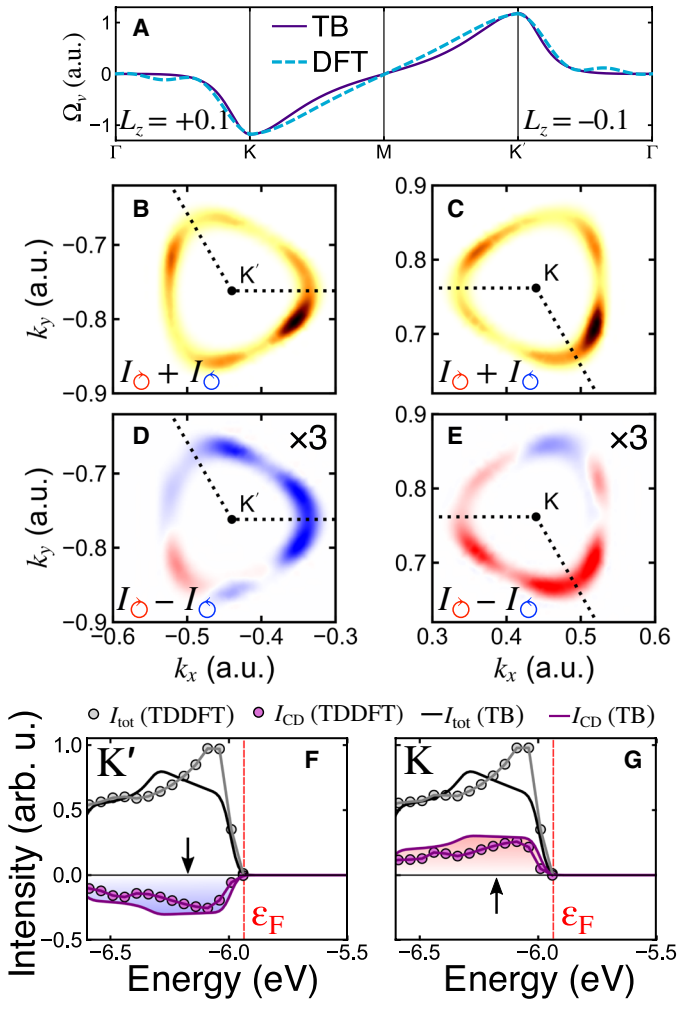

Fig. 3. Berry curvature and circular dichroism in hBN. (**A**) Berry curvature $\Omega_\nu(\mathbf{k})$ of the top valence band, comparing TDDFT and TB results. The angular momentum amounts to $L_z = 0.1$ at K and $L_z = -0.1$ at K′. (**B** and **C**) Total ARPES intensity $I_{\mathrm{tot}}(\mathbf{k},\varepsilon_f)$ at $\varepsilon_f = 45.811$ eV. (**D** and **E**) Corresponding circular dichroism. The color coding is analogous to Fig. 2. (**F** and **G**) The integrated signals as a function of the binding energy at K and K′, respectively.

Figure 3 (B and C) shows the unpolarized signal $I_{tot}(\mathbf{k}, \varepsilon_f)$ for hBN close to the K and K′ points. Note the suppression of the dark corridor, which is due to the incomplete destructive interference.

The corresponding circular dichroism (Fig. 3, D and E) shows, following the behavior of $\Omega_v(\mathbf{k})$ and the OAM, an opposite character at the two inequivalent Dirac points. While irradiating with LCP light results in a much larger probability of creating a photoelectron in the vicinity of the K point, RCP light dominates the emission from the region around K′. Integrating the momentum-resolved signals yields a clear picture (Fig. 3, F and G). The first-principles TDDFT results are qualitatively well reproduced by the TB + PW model, underpinning the intrinsic character of the dichroism.

Bismuthane

To demonstrate the generic character of the connection between the Berry curvature and circular dichroism, we consider single-layer hydrogenated bismuthane (BiH) (see Fig. 4A). Bismuth on the hexagonal lattice is one of most promising candidates for realizing 2D TIs (*16*, *17*) because of its strong intrinsic SOC. A monolayer of hexagonal bismuth has been experimentally characterized on a SiC substrate (*16*). Freestanding bismuth has p_x, p_y, and p_z orbitals contributing to the bands close to the Fermi energy; removing the p_z orbitals from this energy range has been identified as a key mechanism (*17*). The hydrogen atoms fulfill exactly this purpose. The system is slightly buckled, but still has inversion symmetry, such that the spin states are degenerate. Artificially turning off the SOC turns BiH into a Dirac semimetal (Fig. 4B), while the SOC opens a large gap of ≃800 meV at K and K′.

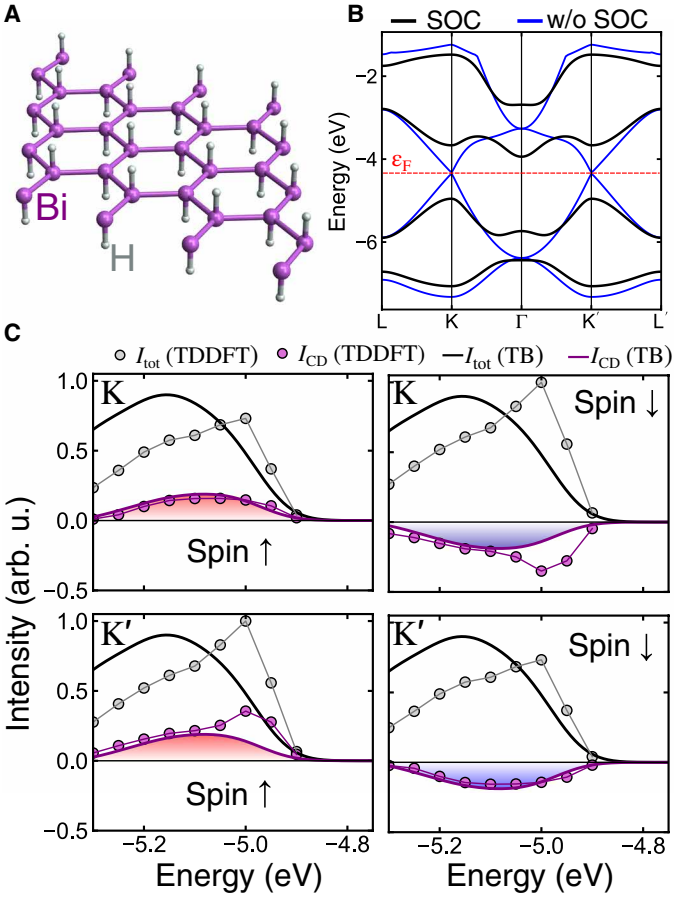

Fig. 4. Circular dichroism in BiH. (**A**) Lattice structure of hexagonal BiH. (**B**) Band structure of hydrogenated bismuthane (BiH; obtained from DFT), fully including SOC (black) and, for the purpose of comparison, without any SOC (blue lines). (**C**) Integrated dichroic signal as in Fig. 2 for spin-up (left panels) and spin-down (right panels) electrons at K (top panels) and K′ (bottom panels), respectively.

Because of the TRS, the Berry curvature (see Fig. 1) is opposite for spin-up and spin-down electrons, respectively. Hence, sARPES is required to distinguish the spin species. Figure 4C shows the integrated (CD-) ARPES signals for both spin channels, in analogy to the non–spin-resolved case of Fig. 3 (F and G). We are focusing on the top valence band. As expected from the case of the TI in Fig. 1, the Berry curvature has the same sign at both K and K′, and so has the orbital polarization. Both quantities are shown explicitly in section S2. The behavior is opposite for spin-up and spin-down, respectively; note that the global TRS implies $I_{CD,\uparrow}(\mathbf{k}, \varepsilon_f) = -I_{CD,\downarrow}(-\mathbf{k}, \varepsilon_f)$. Hence, the integrated circular dichroism has the same sign, confirming that BiH is a spin-Chern insulator. To corroborate the topological nature of the dichroism, we have switched off the SOC within the TB + PW model. We find vanishing valley-integrated dichroism, which is consistent with the signatures of a Dirac semimetal like graphene.

As a second example of a spin-Chern insulator, we can consider graphene. Although SOC is very weak in graphene, it theoretically also renders graphene a spin-Chern insulator (*1*), so it is instructive in this context to study graphene with SOC. However, the SOC-induced gap of ~25 μeV (*44*) is very small, so that graphene in practice behaves like a trivial material, as discussed above. To reveal the dichroic signature of the topologically nontrivial phase, we artificially enhance the SOC by a factor of 500. This allows one to directly observe the impact of the Kane-Mele mechanism (*45*) on the circular dichroism. The opening of the topological gap is shown in Fig. 2B.

The integrated intensities in Fig. 2H show a very good agreement between the full TDDFT calculations and the TB + PW calculations for the unpolarized intensity I_{tot}. The circular dichroism is overestimated by the TB + PW model by a factor of ~20. This indicates that the circular dichroism due to scattering effects (which are missing in the TB + PW model) is competing with the intrinsic dichroism. Nevertheless, the qualitative behavior in both approaches shows a nonvanishing total circular dichroism and thus reveals a topologically nontrivial state.

Universal phase diagram for graphene-like systems

The examples for the three cases of π-conjugate systems discussed above—Dirac semimetal (graphene), trivial insulator (hBN), and TI (graphene with SOC)—can all be described on the TB level by the Haldane model (*46*). The Haldane model is characterized by the gap parameter M, nearest-neighbor hopping J, next–nearest-neighbor hopping J', and the associated phase ϕ. For $M = 2.14J$, $J' = 0$, and $\phi = 0$, the TB model of hBN is recovered, while $M = 0$, $J' = -0.0473J$, and $\phi = \arg(J' - i\lambda)$ correspond to the TB model for graphene with SOC strength λ (*45*).

The good qualitative agreement between the ab initio TDDFT data and the results from the TB + PW model in all considered cases demonstrates the predictive power of the simplified description. Hence, the TB + PW approach may be used to explore the full phase diagram of the Haldane model, providing a comprehensive picture of the circular dichroism in graphene-like systems. For our analysis, we have adopted the parameters and atomic orbitals from graphene, but replaced the TB Hamiltonian by the Haldane model. We have computed the **k**-integrated (over the region shown in Fig. 2B) signal $I_{CD}(K^{(\prime)}, \varepsilon)$, as in Fig. 2, and in addition integrated over the binding

energy ε. The such integrated (but valley-resolved) dichroic signal $S_{CD}(K^{(\prime)}) = \int d\varepsilon\, I_{CD}(K^{(\prime)}, \varepsilon)$ is shown in Fig. 5 (A and B).

As Fig. 5 (A and B) demonstrates, the system exhibits a total dichroism (dominated by LCP light) for $\phi < \pi$ and small enough M. For larger M, the dichroism stays positive around the K point, while it becomes negative at K′. The behavior for $\phi > \pi$ is inverted. This suggests the following measurement strategy: if both $S_{CD}(K) > 0$ and $S_{CD}(K') > 0$, then the system represents a Chern insulator. Similarly, $S_{CD}(K) < 0$ and $S_{CD}(K') < 0$ should correspond to a Chern insulator with opposite Chern number. The case $S_{CD}(K)S_{CD}(K') < 0$ indicates a topologically trivial phase. All these cases can be captured by defining $\Delta S_{CD} = (\text{sign}[S_{CD}(K)] + \text{sign}[S_{CD}(K')])/2$, which is presented in Fig. 5C and compared to the topological phase diagram of the Haldane model.

Figure 5C demonstrates a close relation between the circular dichroism and the topological state, since the region $\Delta S_{CD} = 1$ ($\Delta S_{CD} = -1$) is almost identical to the parameter space with Chern number $C = 1$ ($C = -1$). In contrast, the topologically trivial regime ($C = 0$) is characterized by $\Delta S_{CD} = 0$. The corresponding topological phase diagram shown in Fig. 5C is also consistent with the previous results: the hBN case would be recovered for large enough M (outside the plotted range), while the TB model for graphene with SOC for the spin-up (spin-down) species is equivalent to the Haldane model with $\phi = 17°$ ($\phi = 343°$).

The good agreement between the properties of the CD and the topological phase diagram can be further supported by an analytical evaluation of the TB + PW model (detailed in section S5). Assuming unperturbed atomic orbitals, we explicitly calculate the matrix elements $M^{(\pm)}(\mathbf{k}, p_\perp) = \langle \mathbf{k}, p_\perp | \hat{\epsilon}^{(\pm)} \cdot \mathbf{r} | \psi_{\mathbf{k}\nu} \rangle$ and the asymmetry $\Delta\mathcal{M}(\mathbf{k}, p_\perp) = |M^{(+)}(\mathbf{k}, p_\perp)|^2 - |M^{(-)}(\mathbf{k}, p_\perp)|^2$. This quantity is, up to the energy conservation in Eq. 4, equivalent to the dichroic ARPES intensity. Under these assumptions, one can derive

$$\Delta\mathcal{M}(\mathbf{k}, p_\perp) \propto \sigma_z(\mathbf{k})\,[\mathbf{k} \times \boldsymbol{\tau}]_z\, \tilde{\varphi}(k, p_\perp)\, \partial_k \tilde{\varphi}(k, p_\perp) \qquad (6)$$

where $\boldsymbol{\tau}$ is the vector connecting the sublattice sites, while $\tilde{\varphi}(k, p_\perp)$ is the Fourier transform of the atomic p_z wave function (depending on the modulus $k = |\mathbf{k}|$ only).

The most important term is the orbital pseudospin $\sigma_z(\mathbf{k}) = P_A(\mathbf{k}) - P_B(\mathbf{k})$, measuring the difference in orbital occupation $P_{A,B}(\mathbf{k})$ of the sublattice sites. In a topologically trivial state, only the lower-energy site is predominantly occupied (for instance, the nitrogen site in hBN); hence, $\sigma_z(\mathbf{k}) < 0$ across the whole BZ. Therefore, Eq. 6 yields opposite signs at $\mathbf{k} = K$ and $\mathbf{k} = K'$. In contrast, in a topologically nontrivial state, the orbital inversion leads to a change of sign of $\sigma_z(\mathbf{k})$ in the BZ. In particular, $\sigma_z(K)$ and $\sigma_z(K')$ must have opposite signs. Therefore, the asymmetry (Eq. 6) has the same sign at both K and K′. Hence, the analytical model shows that the total dichroism changes at a topological phase transition.

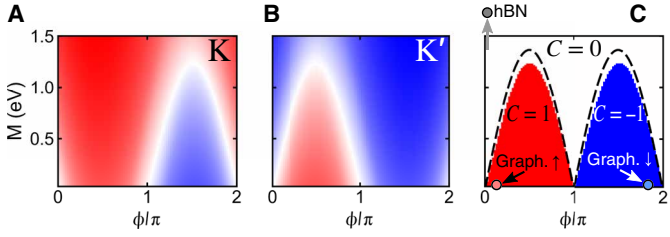

Fig. 5. Circular dichroism and topological phase diagram for the Haldane model. Energy- and valley-integrated circular dichroism S_{CD} around the K (**A**) and K′ (**B**) valley, respectively, as a function of the phase ϕ and gap parameter M. (**C**) Asymmetry signal ΔS_{CD} (see text): red color corresponds to $\Delta S_{CD} = 1$, blue corresponds to $\Delta S_{CD} = -1$, and white corresponds to $\Delta S_{CD} = 0$. The dashed lines represent the critical gap $M_{crit}(\phi)$, for which $M > M_{crit}(\phi)$ turns the system into a trivial insulator. The Chern numbers C are given for each phase. The parameters are analogous to graphene, with $J' = 0.1J$.

DISCUSSION

We have presented a detailed investigation of ARPES and, in particular, the circular dichroism from 2D graphene-like systems. The results were obtained by first-principles calculations of the ARPES intensity based on TDDFT and complemented by the analysis of a simple TB model.

In general, circular dichroism in photoemission can have multiple origins. For instance, interference and scattering effects from the lattice give rise to distinct dichroism. However, in a system having both inversion and TRS (like graphene without SOC), the valley-integrated CD vanishes. Our main focus was not the dichroism related to lattice effects, but that originating from an intrinsic property of the underlying band. This intrinsic contribution is qualitatively captured by the TB model. As the model exhibits only a weak photon energy dependence, such intrinsic dichroic features are expected to be stable against variations of the photon energy.

hBN provides an ideal test case. In this material, the broken inversion symmetry gives rise to a pronounced Berry curvature and associated orbital polarization. The distinct angular momentum at the two inequivalent Dirac points directly translates into a pronounced valley-integrated dichroism. This is supported by the TB model. We stress that the connection between the orbital polarization and the dichroism is more generic and not restricted to graphene-like systems, as confirmed by the example of single-layer BiH. A comprehensive analysis shows that the Berry curvature can be estimated from the orbital polarization if the dominant hybridization gaps are known, even in such multiband systems.

The example of BiH also demonstrates that the TRS breaking associated with the restriction to one spin species results in total dichroism. Analogous effects are present in graphene with enhanced SOC. Hence, measuring circular dichroism from a 2D system allows one to directly determine its topological property, even for a TI with overall TRS. The key aspect is the spin resolution provided by sARPES. This is in contrast to, for instance, optical absorption, which could not distinguish the spin species and would thus result in zero dichroism for spin-Chern insulators, which constitute the majority of existing 2D TIs. Hence, measuring circular dichroism in sARPES provides a powerful tool for the identification of TIs.

A strong influence of topological properties on circular dichroism can be expected for a large class of materials, including mono- and bilayer TMCDs of the type MX_2. As demonstrated in section S6, a direct connection between Berry curvature and orbital polarization also exists for this class of materials. Thus, the valley-topological effects of TMCDs are directly accessible by measuring the circular dichroism in ARPES with its distinct spin and momentum resolution. A recent experimental example is the dichroic spectrum of *2H*-WSe_2 (*38*). The measured circular dichroism matches the calculated Berry curvature, in line with our theory. Another intriguing example is monolayer WTe_2, a nonsymmorphic crystal hosting a topological type II Weyl cone. The measured circular dichroism

has a topological explanation in terms of pseudospin winding (*47*). Hence, our pseudospin picture for circular dichroism is an important step in understanding the signatures of such topological metals.

In full generality, the manifestations of Berry curvature effects in dichroic spectra are intricate. While we found criteria where both quantities can be related to each other (which apply to more systems than studied here), extracting topological properties from a measurement can be a formidable task. For this reason, developing cutting-edge numerical methods and benchmarked models is of great importance for an accurate description of ARPES spectra. The distinct sensitivity of the circular dichroism to topological effects can be exploited in a combined approach based on theory and experiment: only a theoretical description that assumes the correct topological properties can yield dichroic spectra matching experiments. Hence, the feedback between experiments and extensions of our theory will provide insights for more complex materials. Important examples include materials with hidden orbital polarization (*48*), noncollinear spin textures (*34*), and hidden spin polarization (*37*, *49*). Both our ab initio approach and the simplified but accurate modeling provide important insights to guide future experiments.

Furthermore, the extension of ARPES to the time domain (tARPES) (*50*) offers a new way of tracing and defining transient topological phenomena. For instance, the buildup of light-induced topological states (*51*–*56*) should be observable with tARPES in real time. This is particularly important as laser-heating effects typically lead to thermalization at high temperature, where the Hall conductance is not quantized (*57*). In contrast, the energy selectivity of ARPES allows one to identify the topological character of the individual bands, thus providing a conclusive result even in highly excited systems.

MATERIALS AND METHODS

Ab initio ARPES simulations: Numerical details

The evolution of the electronic structure under the effect of external fields was computed by propagating the Kohn-Sham (KS) equations in real space and real time within TDDFT as implemented in the Octopus code (*58*–*61*). We solved the KS equations in the local density approximation with semi-periodic boundary conditions. For all the systems considered, we used a simulation box of 120 a_0 along the nonperiodic dimension and the primitive cell on the periodic dimensions with a grid spacing of 0.36 a_0 and sampled the BZ with a 12×12 **k**-point grid. We modeled graphene with a lattice parameter of 6.202 a_0 and hBN with 4.762 a_0. sARPES was calculated by recording the flux of the photoelectron current over a surface placed 30 a_0 away from the system with the t-SURFFP method (*24*, *62*)—the extension of t-SURFF (*63*) to periodic systems. All calculations were performed using fully relativistic Hartwigsen-Goedecker-Hutter (HGH) pseudopotentials (*64*).

TB modeling

Within the TB model, we approximate the Bloch states $\psi_{\mathbf{k}\alpha}(\mathbf{r})$ by

$$\begin{aligned}\psi_{\mathbf{k}\alpha}(\mathbf{r}) &= \frac{1}{\sqrt{N}}\sum_{\mathbf{R}} e^{i\mathbf{k}\cdot\mathbf{R}}\,\phi_{\mathbf{k}\alpha}(\mathbf{r}-\mathbf{R}) \\ &= \frac{1}{\sqrt{N}}\sum_{\mathbf{R}}\sum_{j} C_{\alpha j}(\mathbf{k})\, e^{i\mathbf{k}\cdot(\mathbf{R}+t_j)}\, w_j(\mathbf{r}-\mathbf{R})\end{aligned} \tag{7}$$

Here, we are using the convention where the phase factor $e^{i\mathbf{k}\cdot\mathbf{t}_j}$ ($\mathbf{t}_j$ denotes the sublattice site positions) is directly included in the definition (Eq. 7) of the Bloch states.

For all considered systems, we have constructed a nearest-neighbor TB model and fitted the onsite and hopping energy to the respective band structure of the DFT calculation. For graphene with enhanced SOC, we have used the next–nearest-neighbor model from (*45*) and fitted the corresponding SOC parameter. For BiH, we used the effective TB Hamiltonian from (*17*) for the subset of p_x and p_y orbitals. In all cases, the band structure obtained by the TB models matches the DFT energies close to the K and K′ point very well.

The TB Wannier orbitals are approximated as

$$w_j^{\gamma}(\mathbf{r}) = C_j \mathbf{u}_{\gamma}\cdot(\mathbf{r}-\mathbf{t})_j \exp\left[-\alpha_j(\mathbf{r}-\mathbf{t}_j)^2\right] \tag{8}$$

where $\mathbf{u}_{\gamma}$ is the unit vector in the direction $\gamma = x, y, z$. The parameters C_j and α_j are fitted to atomic orbitals.

To further simplify the analysis, we approximate the final states as PW. The photoemission matrix elements with respect to the Wannier orbital are evaluated in the length gauge: $M_j(\mathbf{k}, p_{\perp}) = \langle \mathbf{k}, p_{\perp} | \hat{\epsilon}\cdot\mathbf{r} | w_j \rangle$, where the position is measured from the center of the unit cell. More details are presented in section S4.

SUPPLEMENTARY MATERIALS

Supplementary material for this article is available at http://advances.sciencemag.org/cgi/content/full/6/9/eaay2730/DC1

Section S1. SOC effects in graphene and BiH
Section S2. Orbital angular momentum and Berry curvature in multiband systems
Section S3. Wave-packet picture
Section S4. TB modeling of photoemission
Section S5. Pseudospin picture
Section S6. Orbital polarization for monolayer TMDCs
Fig. S1. Spin as quantum number.
Fig. S2. Orbital polarization and Berry curvature of BiH.
Fig. S3. Angular momentum in hBN.
Fig. S4. Topological properties of monolayer TMDCs.

REFERENCES AND NOTES

1. M. Z. Hasan, C. L. Kane, Colloquium: Topological insulators. *Rev. Mod. Phys.* **82**, 3045–3067 (2010).
2. X.-L. Qi, S.-C. Zhang, Topological insulators and superconductors. *Rev. Mod. Phys.* **83**, 1057–1110 (2011).
3. L. Kou, Y. Ma, Z. Sun, T. Heine, C. Chen, Two-dimensional topological insulators: Progress and prospects. *J. Phys. Chem. Lett.* **8**, 1905–1919 (2017).
4. F. D. M. Haldane, Berry curvature on the fermi surface: Anomalous Hall effect as a topological Fermi-liquid property. *Phys. Rev. Lett.* **93**, 206602 (2004).
5. R. Karplus, J. M. Luttinger, Hall effect in ferromagnetics. *Phys. Rev.* **95**, 1154–1160 (1954).
6. F. D. M. Haldane, Geometrical description of the fractional quantum Hall effect. *Phys. Rev. Lett.* **107**, 116801 (2011).
7. T. Neupert, C. Chamon, C. Mudry, Measuring the quantum geometry of Bloch bands with current noise. *Phys. Rev. B* **87**, 245103 (2013).
8. A. Julku, S. Peotta, T. I. Vanhala, D.-H. Kim, P. Törmä, Geometric origin of superfluidity in the Lieb-lattice flat band. *Phys. Rev. Lett.* **117**, 045303 (2016).
9. Y. Li, Y. Rao, K. F. Mak, Y. You, S. Wang, C. R. Dean, T. F. Heinz, Probing symmetry properties of few-layer MoS_2 and h-BN by optical second-harmonic generation. *Nano Lett.* **13**, 3329–3333 (2013).
10. N. Tancogne-Dejean, A. Rubio, Atomic-like high-harmonic generation from two-dimensional materials. *Sci. Adv.* **4**, eaao5207 (2018).
11. E. Barré, J. A. C. Incorvia, S. H. Kim, C. J. McClellan, E. Pop, H.-S. P. Wong, T. F. Heinz, Spatial separation of carrier spin by the valley Hall effect in monolayer WSe_2 transistors. *Nano Lett.* **19**, 770–774 (2019).
12. I. Sodemann, L. Fu, Quantum nonlinear Hall effect induced by berry curvature dipole in time-reversal invariant materials. *Phys. Rev. Lett.* **115**, 216806 (2015).
13. S.-Y. Xu, Q. Ma, H. Shen, V. Fatemi, S. Wu, T.-R. Chang, G. Chang, A. M. M. Valdivia, C.-K. Chan, Q. D. Gibson, J. Zhou, Z. Liu, K. Watanabe, T. Taniguchi, H. Lin, R. J. Cava, L. Fu, N. Gedik, P. Jarillo-Herrero, Electrically switchable Berry curvature dipole in the monolayer topological insulator WTe_2. *Nat. Phys.* **14**, 900–906 (2018).
14. Q. Ma, S.-Y. Xu, H. Shen, D. MacNeill, V. Fatemi, T.-R. Chang, A. M. M. Valdivia, S. Wu, Z. Du, C.-H. Hsu, S. Fang, Q. D. Gibson, K. Watanabe, T. Taniguchi, R. J. Cava, E. Kaxiras, H.-Z. Lu, H. Lin, L. Fu, N. Gedik, P. Jarillo-Herrero, Observation of the nonlinear Hall effect under time-reversal-symmetric conditions. *Nature* **565**, 337–342 (2019).

15. N. Fläschner, B. S. Rem, M. Tarnowski, D. Vogel, D.-S. Lühmann, K. Sengstock, C. Weitenberg, Experimental reconstruction of the berry curvature in a Floquet Bloch band. *Science* **352**, 1091–1094 (2016).
16. F. Reis, G. Li, L. Dudy, M. Bauernfeind, S. Glass, W. Hanke, R. Thomale, J. Schäfer, R. Claessen, Bismuthene on a SiC substrate: A candidate for a high-temperature quantum spin Hall material. *Science* **357**, 287–290 (2017).
17. G. Li, W. Hanke, E. M. Hankiewicz, F. Reis, J. Schäfer, R. Claessen, C. Wu, R. Thomale, Theoretical paradigm for the quantum spin Hall effect at high temperatures. *Phys. Rev. B* **98**, 165146 (2018).
18. A. Marrazzo, M. Gibertini, D. Campi, N. Mounet, N. Marzari, Prediction of a large-gap and switchable Kane-Mele quantum spin Hall insulator. *Phys. Rev. Lett.* **120**, 117701 (2018).
19. D. T. Tran, A. Dauphin, A. G. Grushin, P. Zoller, N. Goldman, Probing topology by heating: Quantized circular dichroism in ultracold atoms. *Sci. Adv.* **3**, e1701207 (2017).
20. M. Schüler, P. Werner, Tracing the nonequilibrium topological state of Chern insulators. *Phys. Rev. B* **96**, 155122 (2017).
21. L. Asteria, D. T. Tran, T. Ozawa, M. Tarnowski, B. S. Rem, N. Fläschner, K. Sengstock, N. Goldman, C. Weitenberg, Measuring quantized circular dichroism in ultracold topological matter. *Nat. Phys.* **15**, 449–454 (2019).
22. T. Cao, M. Wu, S. G. Louie, Unifying optical selection rules for excitons in two dimensions: Band topology and winding numbers. *Phys. Rev. Lett.* **120**, 087402 (2018).
23. I. Souza, D. Vanderbilt, Dichroic *f*-sum rule and the orbital magnetization of crystals. *Phys. Rev. B* **77**, 054438 (2008).
24. U. De Giovannini, H. Hübener, A. Rubio, A first-principles time-dependent density functional theory framework for spin and time-resolved angular-resolved photoelectron spectroscopy in periodic systems. *J. Chem. Theory Comput.* **13**, 265–273 (2017).
25. U. De Giovannini, D. Varsano, M. A. L. Marques, H. Appel, E. K. U. Gross, A. Rubio, Ab initio angle- and energy-resolved photoelectron spectroscopy with time-dependent density-functional theory. *Phys. Rev. A* **85**, 062515 (2012).
26. U. De Giovannini, G. Brunetto, A. Castro, J. Walkenhorst, A. Rubio, Simulating pump-probe photoelectron and absorption spectroscopy on the attosecond timescale with time-dependent density functional theory. *Chem. Phys. Chem.* **14**, 1363–1376 (2013).
27. U. De Giovannini, H. Hübener, A. Rubio, Monitoring electron-photon dressing in WSe_2. *Nano Lett.* **16**, 7993–7998 (2016).
28. H. Hübener, U. De Giovannini, A. Rubio, Phonon driven Floquet matter. *Nano Lett.* **18**, 1535–1542 (2018).
29. S. Fang, R. Kuate Defo, S. N. Shirodkar, S. Lieu, G. A. Tritsaris, E. Kaxiras, Ab initio tight-binding Hamiltonian for transition metal dichalcogenides. *Phys. Rev. B* **92**, 205108 (2015).
30. D. Xiao, M.-C. Chang, Q. Niu, Berry phase effects on electronic properties. *Rev. Mod. Phys.* **82**, 1959 (2010).
31. J. Ma, D. A. Pesin, Chiral magnetic effect and natural optical activity in metals with or without Weyl points. *Phys. Rev. B* **92**, 235205 (2015).
32. C. L. Kane, E. J. Mele, Z_2 topological order and the quantum spin Hall effect. *Phys. Rev. Lett.* **95**, 146802 (2005).
33. T. Okuda, Recent trends in spin-resolved photoelectron spectroscopy. *J. Phys. Condens. Matter* **29**, 483001 (2017).
34. S. R. Park, J. Han, C. Kim, Y. Y. Koh, C. Kim, H. Lee, H. J. Choi, J. H. Han, K. D. Lee, N. J. Hur, M. Arita, K. Shimada, H. Namatame, M. Taniguchi, Chiral orbital-angular momentum in the surface states of Bi_2Se_3. *Phys. Rev. Lett.* **108**, 046805 (2012).
35. Y. Wang, N. Gedik, Circular dichroism in angle-resolved photoemission spectroscopy of topological insulators. *Phys. Stat. Solidi (RRL)* **7**, 64–71 (2013).
36. X. Zhang, Q. Liu, J.-W. Luo, A. J. Freeman, A. Zunger, Hidden spin polarization in inversion-symmetric bulk crystals. *Nat. Phys.* **10**, 387–393 (2014).
37. E. Razzoli, T. Jaouen, M.-L. Mottas, B. Hildebrand, G. Monney, A. Pisoni, S. Muff, M. Fanciulli, N. C. Plumb, V. A. Rogalev, V. . N. Strocov, J. Mesot, M. Shi, J. . H. Dil, H. Beck, P. Aebi, Selective probing of hidden spin-polarized states in inversion-symmetric bulk MoS_2. *Phys. Rev. Lett.* **118**, 086402 (2017).
38. S. Cho, J.-H. Park, J. Hong, J. Jung, B. S. Kim, G. Han, W. Kyung, Y. Kim, S.-K. Mo, J. Denlinger, J. H. Shim, J. H. Han, C. Kim, S. R. Park, Experimental observation of hidden Berry curvature in inversion-symmetric bulk 2*H*–WSe_2. *Phys. Rev. Lett.* **121**, 186401 (2018).
39. W. Schattke, M. A. V. Hove, *Solid-State Photoemission and Related Methods: Theory and Experiment* (John Wiley & Sons, 2008).
40. M. A. L. Marques, N. T. Maitra, F. Nogueira, E. K. U. Gross, A. Rubio, *Fundamentals of Time-Dependent Density Functional Theory* (Springer-Verlag, 2011).
41. C. Hwang, C.-H. Park, D. A. Siegel, A. V. Fedorov, S. G. Louie, A. Lanzara, Direct measurement of quantum phases in graphene via photoemission spectroscopy. *Phys. Rev. B* **84**, 125422 (2011).
42. I. Gierz, M. Lindroos, H. Höchst, C. R. Ast, K. Kern, Graphene sublattice symmetry and isospin determined by circular dichroism in angle-resolved photoemission spectroscopy. *Nano Lett.* **12**, 3900–3904 (2012).
43. Y. Liu, G. Bian, T. Miller, T.-C. Chiang, Visualizing electronic chirality and Berry phases in graphene systems using photoemission with circularly polarized light. *Phys. Rev. Lett.* **107**, 166803 (2011).
44. S. Konschuh, M. Gmitra, J. Fabian, Tight-binding theory of the spin-orbit coupling in graphene. *Phys. Rev. B* **82**, 245412 (2010).
45. C. L. Kane, E. J. Mele, Quantum spin Hall effect in graphene. *Phys. Rev. Lett.* **95**, 226801 (2005b).
46. F. D. M. Haldane, Model for a quantum Hall effect without Landau levels: Condensed-matter realization of the "parity anomaly". *Phys. Rev. Lett.* **61**, 2015 (1988).
47. L. Muechler, A. Alexandradinata, T. Neupert, R. Car, Topological nonsymmorphic metals from band inversion. *Phys. Rev. X* **6**, 041069 (2016).
48. J. H. Ryoo, C.-H. Park, Hidden orbital polarization in diamond, silicon, germanium, gallium arsenide and layered materials. *NPG Asia Mater.* **9**, e382 (2017).
49. W. Yao, D. Xiao, Q. Niu, Valley-dependent optoelectronics from inversion symmetry breaking. *Phys. Rev. B* **77**, 235406 (2008).
50. M. Sentef, A. F. Kemper, B. Moritz, J. K. Freericks, Z.-X. Shen, T. D. Devereaux, Examining electron-boson coupling using time-resolved spectroscopy. *Phys. Rev. X* **3**, 041033 (2013).
51. M. A. Sentef, M. Claassen, A. F. Kemper, B. Moritz, T. Oka, J. K. Freericks, T. P. Devereaux, Theory of Floquet band formation and local pseudospin textures in pump-probe photoemission of graphene. *Nat. Commun.* **6**, 7047 (2015).
52. M. Claassen, C. Jia, B. Moritz, T. D. Devereaux, All-optical materials design of chiral edge modes in transition-metal dichalcogenides. *Nat. Commun.* **7**, 13074 (2016).
53. H. Hübener, M. A. Sentef, U. De Giovannini, A. F. Kemper, A. Rubio, Creating stable Floquet–Weyl semimetals by laser-driving of 3D Dirac materials. *Nat. Commun.* **8**, 13940 (2017).
54. G. E. Topp, N. Tancogne-Dejean, A. F. Kemper, A. Rubio, M. A. Sentef, All-optical nonequilibrium pathway to stabilising magnetic Weyl semimetals in pyrochlore iridates. *Nat. Commun.* **9**, 4452 (2018).
55. M. Claassen, D. M. Kennes, M. Zingl, M. A. Sentef, A. Rubio, Universal optical control of chiral superconductors and Majorana modes. *Nat. Phys.* **15**, 766–770 (2019).
56. J. W. McIver, B. Schulte, F.-U. Stein, T. Matsuyama, G. Jotzu, G. Meier, A. Cavalleri, Light-induced anomalous Hall effect in graphene. arXiv:1811.03522 [cond-mat] (2018).
57. M. Schüler, J. C. Budich, P. Werner, Quench dynamics and Hall response of interacting Chern insulators. *Phys. Rev. B* **100**, 041101(R) (2019).
58. M. A. L. Marques, A. Castro, G. F. Bertsch, A. Rubio, octopus: A first-principles tool for excited electron–ion dynamics. *Comput. Phys. Commun.* **151**, 60–78 (2003).
59. A. Castro, H. Appel, M. Oliveira, C. A. Rozzi, X. Andrade, F. Lorenzen, M. A. L. Marques, E. K. U. Gross, A. Rubio, octopus: A tool for the application of time-dependent density functional theory. *Phys. Stat. Solidi B* **243**, 2465–2488 (2006).
60. X. Andrade, D. Strubbe, U. De Giovannini, A. H. Larsen, M. J. T. Oliveira, J. Alberdi-Rodriguez, A. Varas, I. Theophilou, N. Helbig, M. J. Verstraete, L. Stella, F. Nogueira, A. Aspuru-Guzik, A. Castro, M. A. L. Marques, A. Rubio, Real-space grids and the Octopus code as tools for the development of new simulation approaches for electronic systems. *Phys. Chem. Chem. Phys.* **17**, 31371–31396 (2015).
61. Octopus web page; https://octopus-code.org/wiki/Main_Page.
62. U. De Giovannini, in *Handbook of Materials Modeling* (Springer, Cham, 2018), pp. 1–19.
63. A. Scrinzi, t-SURFF: Fully differential two-electron photo-emission spectra. *New J. Phys.* **14**, 085008 (2012).
64. C. Hartwigsen, S. Goedecker, J. Hutter, Relativistic separable dual-space Gaussian pseudopotentials from H to Rn. *Phys. Rev. B* **58**, 3641 (1998).

Acknowledgments: We acknowledge helpful discussion with P. Tang and T. P. Devereaux. **Funding:** We acknowledge financial support from the Swiss National Science Foundation via NCCR MARVEL and the European Research Council via ERC-2015-AdG-694097 and ERC Consolidator Grant No. 724103. The Flatiron Institute is a division of the Simons Foundation. M.S. thanks the Alexander von Humboldt Foundation for its support with a Feodor Lynen scholarship. M.A.S. acknowledges financial support by the DFG through the Emmy Noether program (SE 2558/2-1). **Author contributions:** M.S. conceived the presented idea, performed the TB calculations and derivations, and wrote the initial draft. U.D.G. and H.H. performed the TDDFT calculations and supported the writing of the manuscript. M.A.S. provided fruitful discussions and supported the writing of the manuscript. A.R. and P.W. supervised the findings of this work. All authors discussed the results and contributed to the final manuscript. **Competing interests:** The authors declare that they have no competing interests. **Data and materials availability:** All data needed to evaluate the conclusions in the paper are present in the paper and/or the Supplementary Materials. Additional data and computer codes related to this paper may be requested from the authors.

Submitted 4 June 2019
Accepted 4 December 2019
Published 28 February 2020
10.1126/sciadv.aay2730

Citation: M. Schüler, U. De Giovannini, H. Hübener, A. Rubio, M. A. Sentef, P. Werner, Local Berry curvature signatures in dichroic angle-resolved photoelectron spectroscopy from two-dimensional materials. *Sci. Adv.* **6**, eaay2730 (2020).

Science Advances

Local Berry curvature signatures in dichroic angle-resolved photoelectron spectroscopy from two-dimensional materials

Michael Schüler, Umberto De Giovannini, Hannes Hübener, Angel Rubio, Michael A. Sentef and Philipp Werner

Sci Adv **6** (9), eaay2730.
DOI: 10.1126/sciadv.aay2730